Processing and Application of Ceramics 18 [4] (2024) 357–365
https://doi.org/10.2298/PAC2404357H

Structural and ferroelectric properties (1-x)($Ba_{0.9}Sr_{0.1}$)TiO_3-xBi($Mg_{2/3}Nb_{1/3}$)O_3 lead-free ceramics with remarkable energy storage performance

Xuechen Huang[1,2,*], Jinba Dai[1], Shulong Liu[3], Wenlong Li[1], Yu Li[1], Wenjun Cao[2], Chunchang Wang[2,*]

[1]*School of Material and Chemical Engineering, Chuzhou University, Chuzhou 239000, PR China*
[2]*Laboratory of Dielectric Functional Materials, School of Material Science and Engineering, Anhui University, Hefei 230601, PR China*
[3]*Anhui Province Industrial Generic Technology Research Center for Alumics Materials, Huaibei Normal University, Huaibei, Anhui 235000, PR China*

Received 3 July 2024; Received in revised form 22 October 2024; Accepted 10 November 2024

Abstract

In this research, (1-x)($Ba_{0.9}Sr_{0.1}$)TiO_3-x Bi($Mg_{2/3}Nb_{1/3}$)O_3 (BST-BMN, where x = 0, 0.06, 0.08, 0.12 and 0.20) powders were synthesized via a solid-state reaction method. The corresponding lead-free ceramics were obtained at the optimal sintering temperature. For x ≥ 0.06, the material formed dense, homogeneous pseudocubic perovskite structures. The increase of the BMN content induces strong relaxor behaviours with diffuse phase transition characteristics, enhancing the temperature stability of dielectric properties. Consequently, the ceramics exhibited narrow polarization-electric field (P-E) loops and superior energy storage capabilities. The composition 0.88BST-0.12BMN was found to be optimal, attributed to the improvement in breakdown field strength, yielding a recoverable energy density of 2.504 J/cm^3 and an efficiency of 90.2% under an electric field strength of 250 kV/cm. Furthermore, this ceramic composition retains consistent energy storage across temperatures ranging from 20 to 120 °C and frequencies from 1 to 100 Hz, underscoring its potential for application in high-power pulsed capacitors.

Keywords: *($Ba_{0.9}Sr_{0.1}$)TiO_3-Bi($Mg_{2/3}Nb_{1/3}$)O_3, dielectric and ferroelectrics properties, energy storage*

I. Introduction

In response to sustainable development imperatives, the urgency of addressing energy storage challenges is intensified. Electrostatic capacitors, supercapacitors and batteries constitute the primary components for electrical energy storage. Notably, dielectric capacitors, due to their high-power density, are extensively used in applications such as electric vehicles, damping technologies, various microwave and electromagnetic devices [1–3]. Nevertheless, the practical application of these capacitors is hindered by their relatively low energy storage capacities. The limitations of low energy density and insufficient overall storage capacity impede their commercialization [4,5]. Enhancing the energy storage density is crucial for meeting the significant demands for power capacitors, with a special emphasis on improving the energy storage capabilities of dielectric materials. Scholarly endeavours are primarily focused on minimizing remanent polarization (P_r), maximizing maximum polarization (P_{max}) and improving electric breakdown strength (E_b) to elevate the overall energy densities of these materials. This targeted approach aims to optimize the performance parameters critical for advancing dielectric ceramics technologies [6,7].

$BaTiO_3$ (BT) based ceramics are prominent lead-free alternatives, favoured for their high maximum polarization (P_{max}) under low electric fields. However, their energy storage capabilities are often limited by low electric breakdown strength (E_b) and high remanent polarization (P_r). Enhancing the energy storage perfor-

*Corresponding author: +86 550 3511052
e-mail: *huangxuechen2007@126.com* (X. Huang)
ccwang@ahu.edu.cn (C. Wang)

mance of BT-based ceramics involves creating solid solutions that disrupt the long-range ferroelectric (FE) order and increase the relaxor behaviour. Integrating BT with $SrTiO_3$, known for its minimal energy loss and high E_b, is one strategic approach [8]. The addition of Sr^{2+} ions disrupts the ferroelectric order, forming polar nanoregions (PNRs), while simultaneously maintaining high P_{max} and reducing P_r. Despite their advantages, (Ba,Sr)TiO_3 (BST) ceramics face challenges such as high sintering temperatures and relatively low E_b, indicating areas for further improvement.

To enhance the performance of BST ceramics in energy storage applications, prior research has explored the addition of Bi(M′,M″)O_3 (where M′ includes Li^+, Mg^{2+}, Zn^{2+}, Ni^{2+}, etc. and M″ comprises Zr^{4+}, Ti^{4+}, Hf^{4+}, Sn^{4+}, Ta^{5+}, Nb^{5+}, etc.) to enhance the electric breakdown strength (E_b) and suppress remanent polarization (P_r) in dielectric ceramics, thereby improving their overall performance. Solid solutions formed between ABO_3 and Bi(M′,M″)O_3 type materials exhibit significant relaxor behaviour and electrical properties, making them highly suitable for energy storage applications. For instance, systems such as $BaTiO_3$-Bi(M′,M″)O_3 [9–12], $Sr_{0.7}Bi_{0.2}TiO_3$-Bi(M′,M″)O_3 [13, 14], $NaNbO_3$-Bi(M′,M″)O_3 [15,16], and $K_{0.5}Na_{0.5}NbO_3$-Bi(M′,M″)O_3 [4,17,18] are noteworthy due to the relaxor behaviour of compounds containing Bi, which effectively reduces P_r and enhances energy storage capabilities. The presence of Bi^{3+} ions in the A-site and complex ions in the B-site disrupts the long-range ferroelectric order, leading to the formation of polar nanoregions [19]. These PNRs significantly broaden and smooth the dielectric-temperature response, contributing to a reduction in remanent polarization and an overall enhancement in the energy storage performance of these ceramics.

It had been reported that (1-x)($Ba_{0.9}Sr_{0.1}$)TiO_3-xBiMeO_3 ceramics exhibited excellent energy storage performance, high effective density and high energy storage efficiency [20,21]. In this study, Bi($Mg_{2/3}Nb_{1/3}$)O_3 was chosen and mixed with $Ba_{0.9}Sr_{0.1}TiO_3$ to form solid solutions. Comprehensive analyses of phase structure, microstructure, dielectric properties and energy storage capabilities were conducted. Results indicated that BMN addition markedly reduced remanent polarization (P_r) and improved electric breakdown strength (E_b), thereby benefiting energy storage density and efficiency. This was attributed to the decreased grain size and enlarged bandgap compared with the pure $Ba_{0.9}Sr_{0.1}TiO_3$. The findings suggest that addition of BMN is an effective strategy to enhance the performance of BST-based ceramics in sophisticated energy storage applications.

II. Experimental

(1-x)($Ba_{0.9}Sr_{0.1}$)TiO_3-xBi($Mg_{2/3}Nb_{1/3}$)O_3 powders, where x = 0, 0.06, 0.08, 0.12, 0.20, were produced via standard solid-state reaction method. Starting materials included $BaTiO_3$ (>99.0%, Guoci Co. Ltd.), Bi_2O_3 (99.8%, Sinopharm Chemical Reagent Co. Ltd.), $SrCO_3$ (>99.0%, Sinopharm Chemical Reagent Co. Ltd.), Nb_2O_5 (>99.5%, Sinopharm Chemical Reagent Co. Ltd.) and MgO (>99.9%, Sinopharm Chemical Reagent Co. Ltd.). The total sample weight was 30 g for each composition. The raw materials for each sample were weighed according to their stoichiometric molar ratios, ensuring that the desired chemical composition was achieved. These components were then mixed with zirconia balls and milled in an alcohol-based solution for 24 h. After calcining at 800 °C for 2 h in air, the powders underwent the second milling process in anhydrous ethanol for 24 h. Subsequently, polyvinyl alcohol (PVA) was added to improve their green strength, resulting in a mixture containing 5% PVA binder. This mixture was then uniaxially pressed under a pressure of approximately 200 MPa to form disks with a thickness of 1–1.5 mm and a radius of 6 mm. The binder was removed by heating to 600 °C, and the disks were subsequently sintered in air at temperatures ranging from 1200 to 1400 °C for 2 h. To mitigate the loss of Bi during sintering, the disks were encased in their original powders.

The bulk densities were measured utilizing the Archimedes' principle with an electronic density balance produced by Shanghai Sunny Hengping Scientific Instrument Co. Ltd. The phase purity and crystallinity were assessed using a Bruker D8 ADVANCE X-ray powder diffractometer (XRD) with a 2θ range of 10° to 80° operating at 40 kV and 40 mA with Cu Kα radiation (λ = 1.54056 Å, Bruker, Germany). The sintered ceramic samples were ground into powder for XRD measurement. The morphology of the samples was scrutinized using a JEOL JSM-6510A scanning electron microscope (SEM, Japan) at an applied voltage of 20 kV and a magnification of 5000–12000×. Prior to conducting dielectric measurements, the surfaces of the sintered ceramics were polished to ensure they were parallel and smooth. Electrodes were created by applying a silver paste and undergoing a co-firing process at 500 °C for 10 min. The variation in dielectric properties with temperature was comprehensively evaluated using a Wayne Kerr 6500B impedance analyser and a DMS-2000 dielectric detector in Wuhan, China, over a temperature range of −100 to 250 °C, while sweeping the frequency from 100 Hz to 1 MHz. For energy storage evaluations, the 0.15 mm thick polished specimens were outfitted with Au electrodes of a 1 mm radius. Lastly, the polarization-electric (P-E) field response was investigated using a MultiFerroic II ferroelectric hysteresis device (Radiant Technologies Inc.) positioned in a silicone oil bath to facilitate measurements across various frequencies and temperatures.

III. Results and discussion

3.1. Structural characterization

Bulk densities of the (1-x)BST-xBMN ceramics (with x ranging from 0 to 0.20) sintered within a temperature

range of 1125 to 1375 °C are shown in Fig. 1. These data were used to find the optimum sintering temperatures for final ceramics. For the undoped BST ceramics, high bulk densities are achieved within the temperature range of 1300–1375 °C. As the BMN content increases to x = 0.06 and 0.08, the optimal sintering temperature range remains broad, with peak bulk densities achieved between 1175 and 1325 °C. Furthermore, for the compositions with higher BMN fractions, ranging from x = 0.12 to 0.20, the optimal sintering temperatures are even lower, spanning from 1125 to 1250 °C. At these temperatures, the ceramics exhibit remarkable bulk densities, indicating the inverse relationship between optimal sintering temperature and BMN content. This trend can be attributed to the presence of Bi_2O_3 in BMN, which has a low melting point. During sintering, Bi_2O_3 promotes the formation of a liquid phase that enhances mass transport and accelerates pore elimination [22]. Consequently, faster densification occurs at lower temperatures, leading to improved bulk densities.

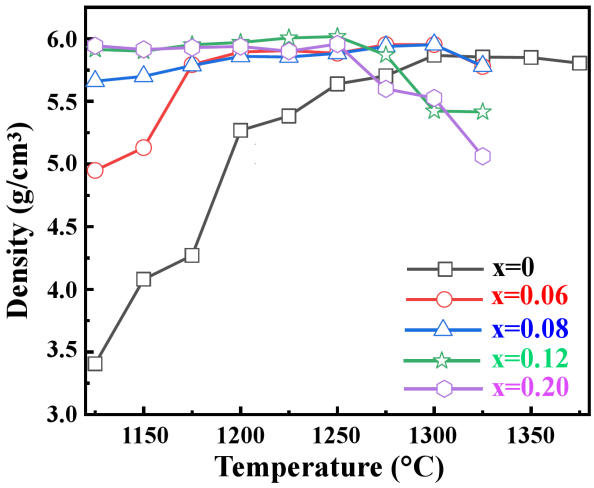

Figure 1. Bulk density of (1-x)BST-xBMN (x = 0–0.20) ceramic powders

Room temperature XRD patterns (Fig. 2) of the ceramic powders (1-x)BST-xBMN (where x ranges from 0 to 0.20) show a stable perovskite phase in all cases. The XRD analysis verified that the undoped $(Ba_{0.9}Sr_{0.1})TiO_3$ samples possess tetragonal symmetry, whereas samples with $x \geq 0.06$ exhibit cubic symmetry. The shift of peak positions towards lower angles indicates lattice expansion as the BMN content increases. For $(Ba_{0.9}Sr_{0.1})TiO_3$, the average ionic radius at the A-site (12-fold coordination) was calculated using the formula $r = 0.1 \times r_{Sr^{2+}} + 0.9 \times r_{Ba^{2+}}$. Since ionic radii of Sr^{2+} and Ba^{2+} are 1.44 Å and 1.61 Å, respectively, the calculated average ionic radius is 1.59 Å. Thus, Bi^{3+} has a smaller ionic radius (1.17 Å) than the calculated value of 1.59 Å. On the other hand, the ionic radii of Mg^{2+} and Nb^{5+} were 0.693 Å, respectively, thus the average ionic radius for $Bi(Mg_{2/3}Nb_{1/3})O_3$ at the B site (6-fold coordination) calculated using $r = 2/3 \times r_{Mg^{2+}} + 1/3 \times r_{Nb^{5+}}$ was

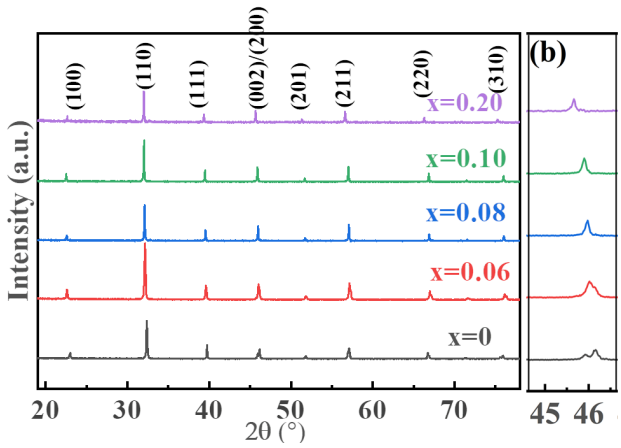

Figure 2. X-ray diffraction patterns of (1-x)BST-xBMN (x = 0–0.20) ceramic powders (a) and enlarged from 44.6 to 46.7 for $0 \leq x \leq 0.20$ (b)

0.693 Å. Thus, the calculated ionic radius of 0.693 Å is larger than that of Ti^{4+} (0.605 Å) at 6-fold coordination. In the perovskite structure, the A–O bond length can be approximately regarded as the sum of the effective ionic radii of the A ion and the O ion, similarly, the B–O bond length can also be approximately estimated by summing the effective ionic radii of the B ion and the O ion [23]. The tolerance factor t of 1 and r_B/r_O of 0.425 typically signify an ideal perovskite structure [24]. It is well known that the octahedron BO_6 serves as the basic mosaic or unit for the perovskite structure. If one cation and six anions form an octahedron, the ratio of their ionic radii (r_B/r_O) is reported within a limited range [25]. In ABO_3-type perovskite, the ratio of the A and B ionic radii (r_A/r_B) within the range of 1.5099 to 2.563 signifies the perovskite structure, and the electronegativity difference between B and O is greater than 1.42 [26]. The tolerance factors are 0.738 for Mg^{2+}/Nb^{5+} substitution at the A-site, 1.01 at the B-site, and 0.907 for Bi^{3+} substitution at the A-site and 0.823 at the B-site. Bi^{3+} (1.17 Å) is significantly larger than Ti^{4+} (0.605 Å). Ratios r_B/r_O are 0.495 and 0.827 for Mg^{2+}/Nb^{5+} and Bi^{3+} substitution at the B-site, respectively. Ratios r_A/r_B are 1.934 for Bi^{3+} substitution at the A-site and 1.359 at the B-site, whereas r_A/r_B are 1.145 for Mg^{2+}/Nb^{5+} substitution at the A-site and 2.294 at the B-site. Predominantly, Bi^{3+} and Mg^{2+}/Nb^{5+} ions are more likely to substitute for Ba^{2+} at the A-site and Ti^{4+} at the B-site, respectively. This suggested that the unit cell expansion of the (1-x)BST-xBMN perovskite structure is mainly governed by the BO_6 octahedra. The possible substitution reactions can be shown as below [27,28]:

$$Bi_2O_3 \xrightarrow{2\,BaO} 2\,Bi_{Ba}^{\bullet} + 2\,O_O + O_i'' \quad (1)$$

$$Bi_2O_3 \xrightarrow{2\,SrO} 2\,Bi_{Sr}^{\bullet} + 2\,O_O + O_i'' \quad (2)$$

$$MgO \xrightarrow{TiO_2} Mg_{Ti}'' + O_O + V_i^{\bullet\bullet} \quad (3)$$

$$Nd_2O_5 \xrightarrow{2\,TiO_2} 2\,Nd_{Ti}^{\bullet} + 4\,O_O + O_i'' \quad (4)$$

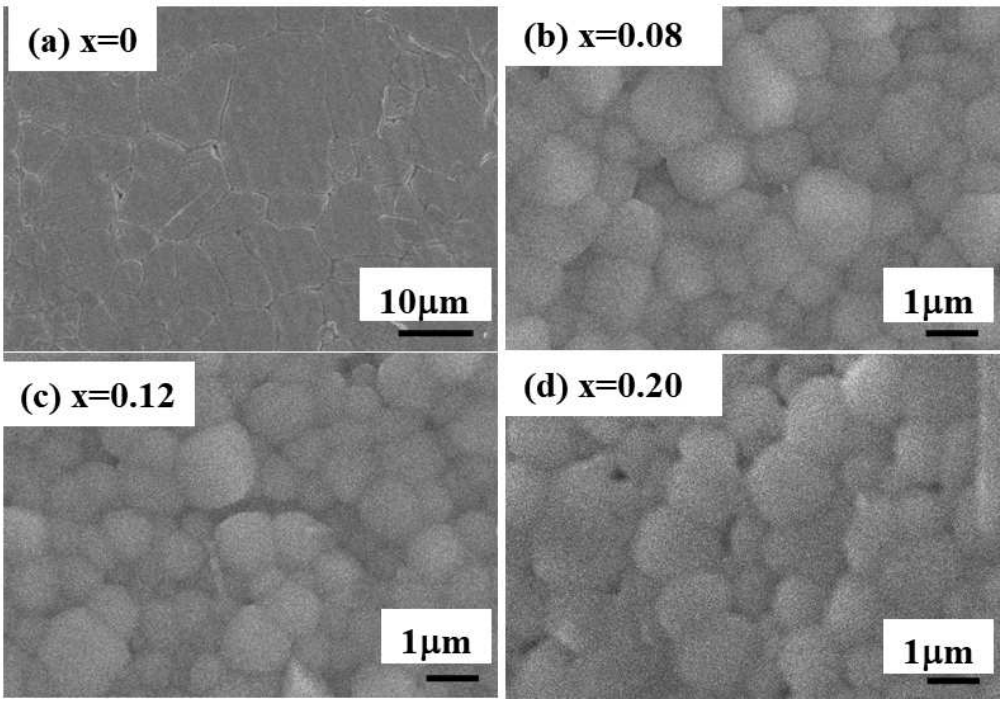

Figure 3. SEM images of thermally-etched surfaces for (1-*x*)BST-*x*BMN ceramics, where *x* is: a) 0, b) 0.08, c) 0.12 and d) 0.20

Bi^{3+} and Mg^{2+}/Nb^{5+} substitution may introduce certain defect types as shown above, resulting in higher solubility in BST ceramics [29]. Therefore, the addition of BMN to BST results in the (002) and (200) peaks merging, and also the peak shifting towards lower angles [30,31].

Figure 3 depicts the SEM surface morphology of the (1-*x*)BST-*x*BMN ceramics (x = 0–0.20), each sintered at their respective optimal temperatures (1300 °C for the samples having x = 0, 0.06 and 0.08, and 1250 °C for the samples with x = 0.12 and 0.20). The undoped BST ceramics exhibit polygonal grains, which is consistent with previously reported literature [32,33]. Additionally, the undoped BST ceramics exhibited a notably large average grain size [21,32].

Figure 4 displays the statistical distribution of grain

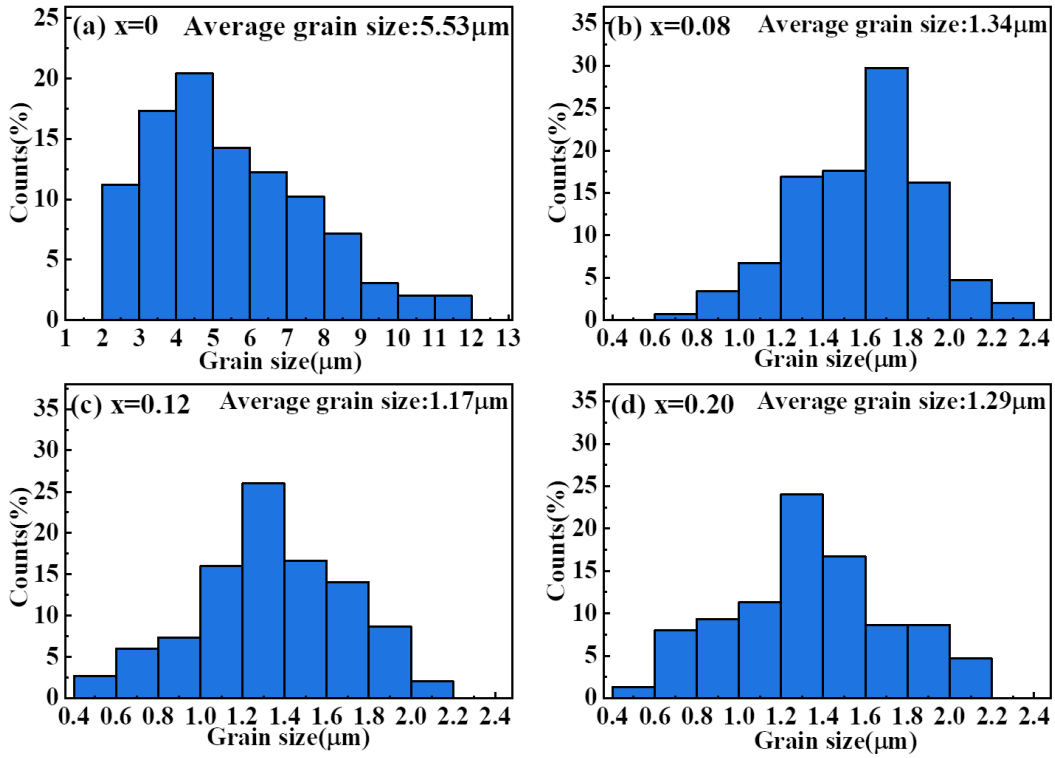

Figure 4. Grain size distribution of (1-*x*)BST-*x*BMN ceramics, where *x* is: a) 0, b) 0.08, c) 0.12 and d) 0.20

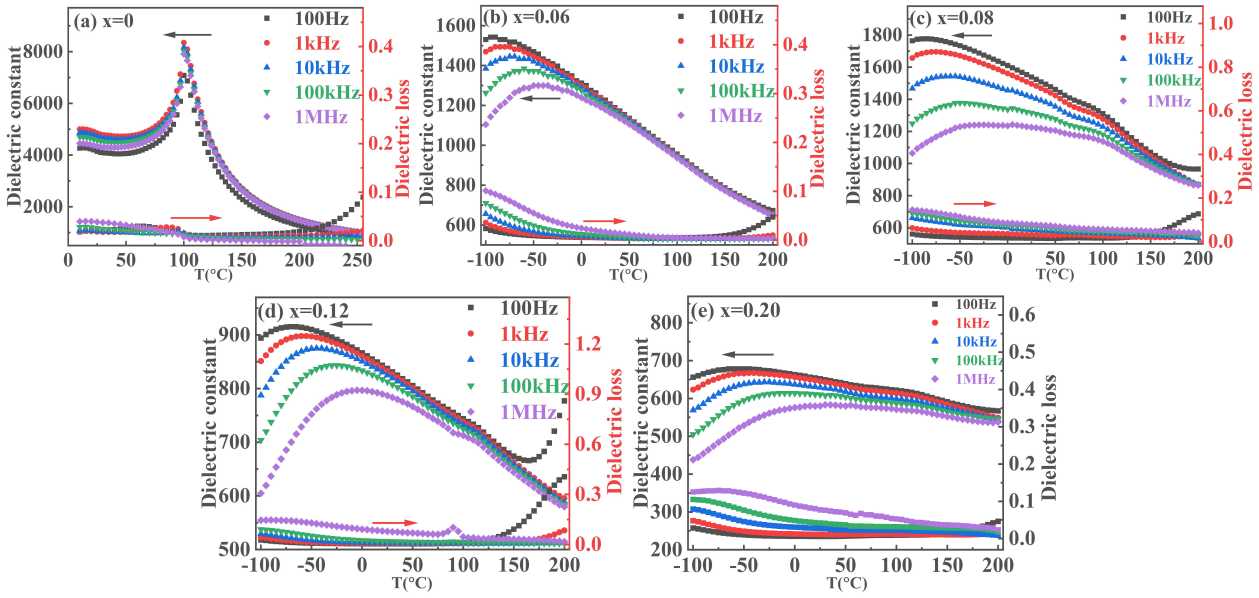

Figure 5. Dielectric constant and dielectric loss as functions of temperature at frequencies from 1 kHz to 1 MHz in (1-*x*)BST-*x*BMN ceramics, where *x* is: a) 0, b) 0.06, c) 0.08, d) 0.12 and e) 0.20

sizes for the (1-*x*)BST-*x*BMN ceramics, analysed using Nano Measurer software, offering insights into the influence of varying BMN content levels. The average grain sizes for the (1-*x*)BST-*x*BMN ceramics were approximately 5.53 μm for $x = 0$, decreasing to 1.17 μm for $x = 0.12$ and slightly increasing to 1.29 μm for $x = 0.20$. The reduction in grain size is primarily attributed to the lower sintering temperatures and a decrease in oxygen vacancies [20]. A slight increase in grain size, from 1.17 μm to 1.29 μm, was observed as the BMN concentration increased from 0.12 to 0.20. This increase is due to the enhanced liquid phase formation during sintering at higher BMN levels, facilitating grain growth [33]. The liquid phase plays a dominant role in the sintering process. Furthermore, SEM observations support the XRD findings, revealing no evidence of a secondary phase.

3.2. *Dielectric and ferroelectrics properties*

The temperature-dependent dielectric properties of the (1-*x*)BST-*x*BMN ($x = 0$–0.20) lead-free ceramics across various frequencies are depicted in Fig. 5. The addition of BMN to BST led to a rapid decline in the characteristic dielectric peaks and a significant decrease in the maximum dielectric constant. Furthermore, the Curie peaks shifted to lower temperatures and broadened, suggesting a transition from conventional ferroelectric behaviour to a more diffuse and dispersive relaxor-like behaviour. The occurrence of diffusion phase transition and frequency dispersion demonstrates that BMN modified BST ceramics exhibit typical relaxation behaviour, which is due to the occupation of similar positions in the crystal by different cations, resulting in the destruction of the long-range ordered structure of ferroelectrics [34,35]. In (1-*x*)BST-*x*BMN ceramics,

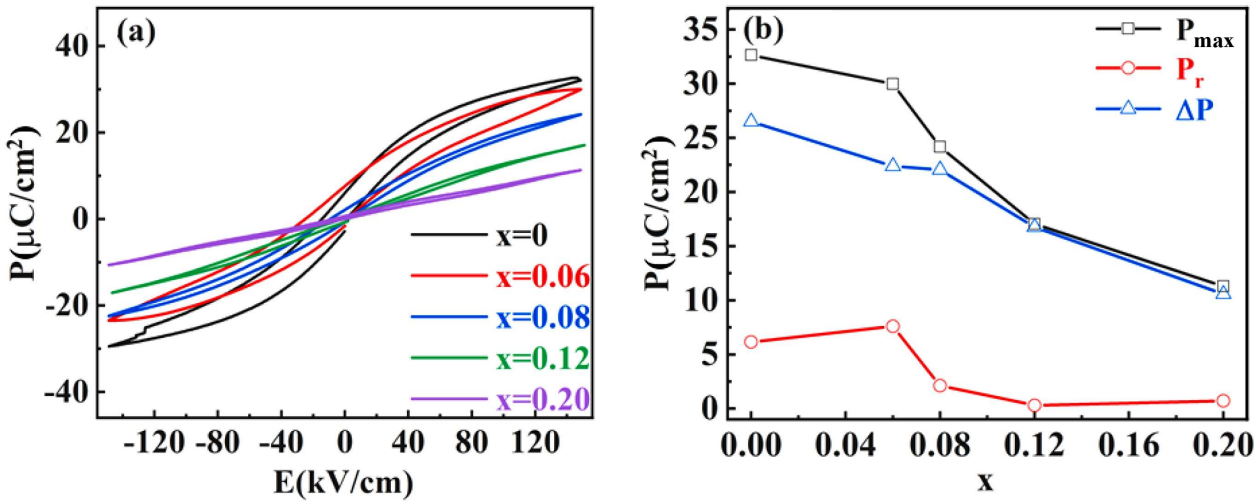

Figure 6. *P-E* loops (a) and P_r, P_{max} and ΔP (b) of (1-*x*)BST-*x*BMN ceramics ($x = 0$–0.20) at the electric field of 150 kV/cm

Ba^{2+} and Sr^{2+} at the A site were replaced by Bi^{3+}, while Ti^{4+} was replaced by Mg^{2+} and Nb^{5+}, leading to lattice structure distortion and local charge imbalance, which results in PNRs that participate in relaxation behaviour. The XRD results reveal pseudocubic phase characteristics in the $x \geq 0.06$ composites, which are consistent with the observed relaxor-like behaviour. The pseudocubic phase indicates a structural complexity and inhomogeneity within the material, which can facilitate the formation of nanodomains and contribute to the diffuse and dispersive nature of the dielectric response [32]. This relaxor behaviour is analogous to that observed in other $BaTiO_3$-$BiMeO_3$ systems [11] and is attributed to the enhanced combined effect arising from the substitution of Mg^{2+}/Nb^{5+} at the Ti-site and Bi^{3+} at the Ba/Sr-site.

To assess the energy storage density of the BMN-substituted specimens, hysteresis loops were acquired for the (1-x)BST-xBMN ceramics (x = 0–0.20) sintered at their respective optimal temperatures at a constant electric field of ~150 kV/cm, 10 Hz and ambient temperature (Fig. 6). Hysteresis loops with a high P_r were observed for the samples with $x = 0$. For $x \geq 0.06$, P-E loops became progressively slimmer and more linear, indicative of paraelectric behaviour likely due to the increased cation disorder from Bi^{3+} substitution at A-sites and Mg^{2+}/Nb^{5+} at B-sites. Ionic size and charge variations weakened long-range dipole interactions due to the local polar distortions in nanoregions [19]. The formation of discrete PNRs stems from weak inter-cluster coupling, a consequence of compositional non-uniformity and charge variance, crucial for relaxor behaviour [36]. P_{max} decreased with higher BMN concentrations.

Fundamental principles dictate that the energy density and efficiency of dielectric ceramics are quantified by established equations [37]:

$$W = \int_0^{P_{max}} E \cdot \mathrm{d}P \tag{5}$$

$$W_{rec} = \int_{P_r}^{P_{max}} E \cdot \mathrm{d}P \tag{6}$$

$$\eta = \frac{W_{rec}}{W} \cdot 100\% \tag{7}$$

where W, W_{rec} and η signify the energy storage density, recoverable energy storage density and energy storage efficiency, respectively, E symbolizes the applied electric field, while P_{max} and P_r denote the remanent and maximum polarizations, respectively.

Values of W, W_{rec} and η, calculated for all samples using Eqs. 5–7, are shown in Fig. 7. η and W_{rec} initially decreased and increased as BMN content rose from 0 to 0.12. At a BMN concentration of 0.12, η peaked at 92.7%. Energy storage density (W) declined with increased BMN amount. On the other hand, W_{rec} was slightly higher at $x = 0.08$ compared to $x = 0.12$ (1.392 vs. 1.129 J/cm^3). Thus, η and E_b were more favourable at $x = 0.12$ ($\eta = 90.2\%$, $E_b = 250$ kV/cm) than at $x = 0.08$ ($\eta = 85.1\%$, $E_b = 200$ kV/cm), enhancing energy storage capability. This enhancement of properties is attributed to the beneficial effects of BMN which enhances the structural distortion due to the lone-pair electrons on Bi^{3+} and the ferroelectrically active Mg^{2+} and Nb^{5+}, and to the enhanced relaxor behaviour arising from the increase of the local disorder and nanodomains effect.

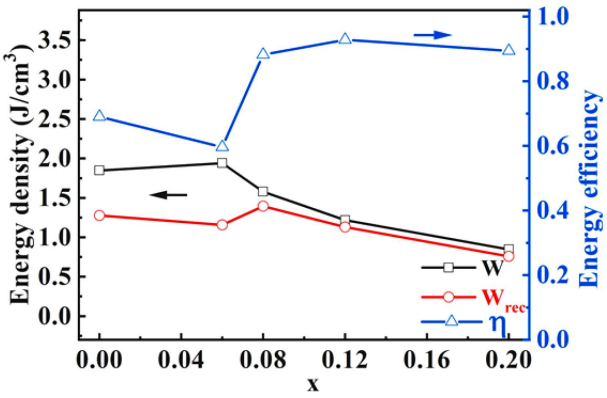

Figure 7. W, W_{rec} and η at the electric field of 150 kV/cm of (1-x)BST-xBMN ceramics (x = 0–0.20)

To rigorously evaluate the applicability of the 0.88BST-0.12BMN ceramics in practical energy storage, the dependence of its energy storage properties on frequency, temperature and electric field is presented in Fig. 8. Figure 8a illustrates the P-E loops of the 0.88BST-0.12BMN at an electric field of 100 kV/cm and room temperature over a frequency range of 1–100 Hz, exhibiting minimal frequency dependence. P_{max}, P_r and ΔP exhibited a little change within a frequency range of 1–100 Hz (Fig. 8c). Correspondingly, the calculated W_{rec} (1.101 to 1.193 J/cm^3) and η (88.3% to 94.4%) remain stable within a frequency range of 1–100 Hz (Fig. 8b). Notably, at the investigated temperatures, a slender P-E loop is observed, with both P_{max} and P_r exhibiting a marginal decrease as the temperature increases. As depicted in Fig. 8e, the calculated energy storage parameters of the 0.88BST-0.12BMN reveal that W_{rec} ranges from 1.096 to 1.176 J/cm^3 and η remains high, between 90.5% and 92.5%, across a broad temperature range. These findings imply that the ergodic relaxor phases remain stable within the measured temperature intervals [38]. Figures 8g and 8i respectively illustrate the P-E loops and the values of P_{max}, P_r, and ΔP ($P_{max} - P_r$) at 10 Hz and room temperature under different electric fields. It is evident that P_{max} and ΔP significantly increase as the electric field amplitude is augmented. Concurrently, a minor rise in P_r suggests that elevating the applied electric field notably enhances W_{rec} while maintaining a high η. To substantiate this observation, Fig. 8h presents the computed energy storage metrics of W, W_{rec} and η for the 0.88BST-0.12BMN under different electric fields. It is observed that the W_{rec} significantly increases, ranging from 1.110

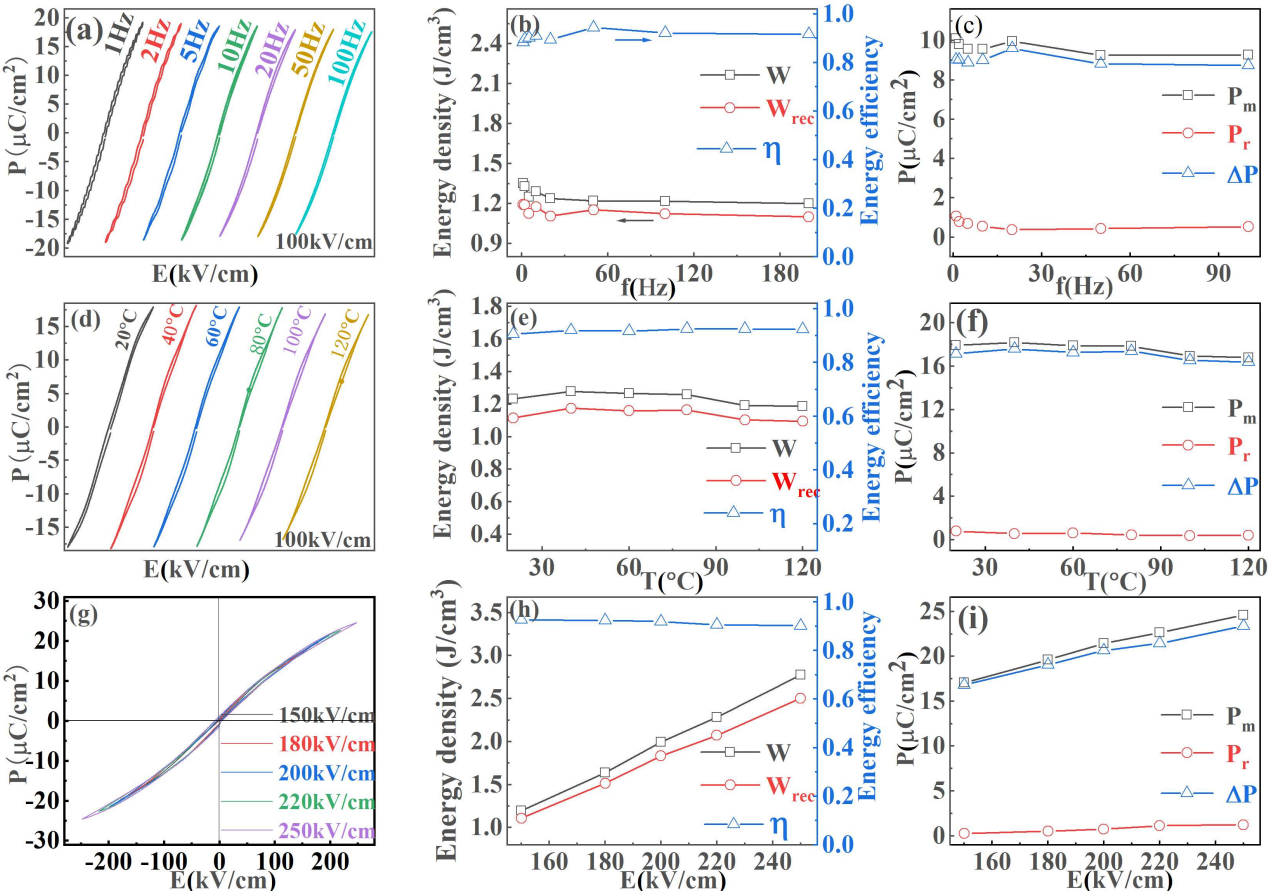

Figure 8. ***P-E*** **loops (a,d,g),** ***W***, W_{rec} **and** η **(b,e,h) and** P_m, P_r **and** ΔP **(c,f,i) for 0.88BST-0.12BMN ceramics at different frequencies (a,b,c), temperatures (c,d,e) and electric fields (g,h,i)**

to 2.504 J/cm^3, while there is a slight reduction in η, from 92.7% to 90.2%, correlating with an increment in electric field strength from 150 to 250 kV/cm. This finding confirms that the 0.88BST-0.12BMN exhibits high W_{rec} and consistently high η within medium electric field ranges.

IV. Conclusions

This study focuses on synthesizing lead-free (1-*x*)BST-*x*BMN ceramics using conventional solid-state method, assessing their crystallographic phases, microstructures, dielectric properties, and energy storage capabilities in detail.

X-ray diffraction has confirmed the complete integration of BMN into the BST matrix. (1-*x*)BST-*x*BMN ceramics presented highly diffuse dielectric peaks and temperature-stable dielectric constant over a temperature range from −100 to 200 °C for different *x* values. The addition of BMN results in the reduction of grain size. This alteration significantly enhances the electric breakdown strength (E_b) to 250 kV/cm, and achieves a recoverable energy storage density (W_{rec}) of 2.504 J/cm^3 with an efficiency (η) of 90.2% at $x = 0.12$. The ceramics exhibit remarkable frequency and temperature stability, enhancing their suitability for advanced energy storage systems. These findings emphasize the enhanced energy storage properties of ceramics, underscoring their potential for application in sophisticated energy storage systems.

Acknowledgements: This work was supported by the University Synergy Innovation Program of Anhui Province (GXXT-2022-086); the Natural Science Key Project of Anhui Education Department (2024AH051406), the Natural Science Youth Foundation of Anhui Province (1808085QE153); University's scientific research project (zrjz2021014); University Students' Innovation and Entrepreneurship Program (2023CXXL20508). University Students' Innovation and Entrepreneurship Program (2024CXXL019).

References

1. W. Cao, R. Lin, X. Hou, L. Li, F. Li, D. Bo, B. Ge, D. Song, J. Zhang, Z. Cheng, C. Wang, "Interfacial polarization restriction for ultrahigh energy-storage density in lead-free ceramics", *Adv. Funct. Mater.*, **33** [29] (2023) 2301027.
2. F. Lv, X. Jiang, L. Zhou, Z. Hong, Y. Wu, Y. Huang, "Enhanced energy storage performance and theoretical understanding of the dielectric breakdown behavior for $Ba_{0.4}Sr_{0.6}TiO_3/Al_2O_3$ ceramics", *J. Alloys Compd.*, **923** (2022) 166344–166353.
3. K. Merve, A. Umut, "Enhanced room temperature energy storage density of $Bi(Li_{1/3}Ti_{2/3})O_3$ substituted $Bi_{0.5}Na_{0.5}TiO_3$-$BaTiO_3$ ceramics", *J. Phys. D*, **54** [27]

(2021) 275501–275511.
4. R. Hu, Y. Lin, M. Zhang, Q. Yuan, H. Yang, "Enhancement of recoverable energy density and efficiency of $K_{0.5}Na_{0.5}NbO_3$ ceramic modified by $Bi(Mg_{0.5}Zr_{0.5})O_3$", *Mater. Today Energy*, **30** (2022) 101185.
5. H. Liu, Z. Sun, J. Zhang, H. Luo, Y. Yao, X. Wang, H. Qi, S. Deng, J. Liu, L.C. Gallington, Y. Zhang, N.C. Joerg, J. Chen, "Local chemical clustering enabled ultrahigh capacitive energy storage in Pb-free relaxors", *J. Am. Chem. Soc*., **145** [35] (2023) 19396–19404.
6. S. Zhou, Y. Pu, X. Zhang, Y. Shi, Z. Gao, Y. Feng, G. Shen, X. Wang, D. Wang, "High energy density, temperature stable lead-free ceramics by introducing high entropy perovskite oxide", *Chem. Eng. J*., **427** (2022) 131684.
7. N. Luo, L. Ma, G. Luo, C. Xu, L. Rao, Z. Chen, Z. Cen, Q. Feng, X. Chen, F. Toyohisa, Y. Zhu, J. Hong, J. Li, S. Zhang, "Well-defined double hysteresis loop in $NaNbO_3$ antiferroelectrics", *Nat. Commun*., **14** [1] (2023) 1776.
8. S. Chao, F. Dogan, "$BaTiO_3$-$SrTiO_3$ layered dielectrics for energy storage", *Mater. Lett*., **65** [6] (2011) 978–981.
9. C. Ma, R. Zhang, G. Zhang, H. Du, J. Liu, R. Liang, Z. Wang, "Structural evolution and energy storage properties of $Bi(Zn_{0.5}Zr_{0.5})O_3$ modified $BaTiO_3$-based relaxation ferroelectric ceramics", *J. Energy Storage*, **72** (2023) 108374.
10. H. Zhao, X. Yang, D. Pang, X. Long, "Enhanced energy storage efficiency by modulating field-induced strain in $BaTiO_3$-$Bi(Ni_{2/3}Ta_{1/3})O_3$ lead-free ceramics", *Ceram. Int*., **47** [16] (2021) 22734–22740.
11. Z. Liu, M. Li, Z. Tang, X. Tang, "Enhanced energy storage density and efficiency in lead-free $Bi(Mg_{1/2}Hf_{1/2})O_3$-modified $BaTiO_3$ ceramics", *Chem. Eng. J*., **418** (2021) 129379.
12. F. Si, B. Tang, Z. Fang, H. Li, S. Zhang, "A new type of $BaTiO_3$-based ceramics with $Bi(Mg_{1/2}Sn_{1/2})O_3$ modification showing improved energy storage properties and pulsed discharging performances", *J. Alloys Compd*., **819** (2020) 153004.
13. M.A. Khan, A. Manan, M.U. Rehman, S. Faisal, A.H. Shah, H.U. Shah, F. Alresheedi, Z.A. Ghazi, S.U. Khan, "Enhanced energy storage characteristics of $Bi(Mg_{0.5}Ce_{0.5})O_3$ modified $(Sr_{0.7}Bi_{0.2})TiO_3$ lead-free ceramics", *J. Mater. Eng. Perform*., **33** [3] (2023) 1538–1547.
14. X. Kong, L. Yang, Z. Cheng, S. Zhang, "Enhanced energy-storage properties and good temperature stability in $0.92(Sr_{0.7}Bi_{0.2})TiO_3$-$0.08Bi(Mg_{0.5}Hf_{0.5})O_3$ relaxor ferroelectric ceramic", *Adv. Energy Sustain. Res*., **2** [6] (2021) 2100015.
15. S. Zhang, W. Li, Y. Zhang, X. Tang, Y. Jiang, X. Guo, "Large energy density and high efficiency achieved simultaneously in $Bi(Mg_{0.5}Hf_{0.5})O_3$-modified $NaNbO_3$ ceramics", *Results Phys*., **44** (2023) 106194.
16. R. Shi, Y. Pu, W. Wang, X. Guo, J. Li, M. Yang, S. Zhou, "A novel lead-free $NaNbO_3$-$Bi(Zn_{0.5}Ti_{0.5})O_3$ ceramics system for energy storage application with excellent stability", *J. Alloys Compd*., **815** (2020) 152356.
17. M. Zhang, H. Yang, Y. Yu, Y. Lin, "Energy storage performance of $K_{0.5}Na_{0.5}NbO_3$-based ceramics modified by $Bi(Zn_{2/3}(Nb_{0.85}Ta_{0.15})_{1/3})O_3$", *Chem. Eng. J*., **425** (2021) 131465.
18. D. Sushmita, P. Tanvi, K. Sunil "Structure, dielectric, and piezoelectric properties of $K_{(0.5)}Na_{(0.5)}NbO_{(3)}$-based lead-free ceramics", *RSC Adv*., **8** [43] (2018) 24286–24296.
19. X. Huang, S. Li, C. Wang, H. Long, P. Chen, F. Xiao, Y. Chen, "Structural, dielectric, and ferroelectric properties of $BaTiO_3$-$Bi(Ni_{1/2}Ti_{1/2})O_3$ lead-free ceramics with remarkable energy storage performance under low electric fields", *J. Mater. Sci. Mater. Electron*., **33** [13] (2022) 10042–10056.
20. B. Moharana, S. Anwar, S. Anwar, "Effect of Zr substitution on electrical properties of $Ba_{0.9}Sr_{0.1}Ti_{1-x}Zr_xO_3$ ($0 \leq x \leq 0.20$) ceramics", *Mater. Sci. Eng. B*, **288** (2023) 116200.
21. Z. Xia, Y. Pan, Y. Chen, Z. Xu, "Enhanced energy storage properties of $Bi(Mg_{0.5}Zr_{0.5})O_3$ modified $Ba_{0.9}Sr_{0.1}TiO_3$ ceramics", *Cryst. Res. Technol*., **58** [2] (2022) 2200147.
22. X. Huang, B. Liu, H. Liu, S. Wang, Y. Liu, G. Liu, "Effects of Bi_2O_3 and MgO on microstructure and dielectric properties of $BaTiO_3$-$(Na_{1/4}Bi_{3/4})(Mg_{1/4}Ti_{3/4})O_3$ system", *J. Mater. Sci. Mater. Electron*., **30** (2019) 10651–10659.
23. J. Liu, K. Ren, C. Ma, H Du, Y. Wang, "Dielectric and energy storage properties of flash-sintered high-entropy $(Bi_{0.2}Na_{0.2}K_{0.2}Ba_{0.2}Ca_{0.2})TiO_3$ ceramic", *Ceram. Inter*., **46** [12] (2020) 20576–20581.
24. Z. Wang, Z. Kang, *Functional and Smart Materials*, Plenum Press, New York, 1998.
25. C.H. Li, K.C. K. Soh, P. Wu, "Formability of ABO_3 perovskites", *J. Alloys Compd*., **372** (2004) 40–48.
26. P.V. Balachandran, S.R. Broderick, K. Rajan, "Identifying the 'inorganic gene' for high-temperature piezoelectric perovskites through statistical learning", *Proc. R. Soc. A*, **467** (2011) 2271–2290.
27. Y. Yan, C. Ning, Z. Jin, H. Qin, W. Luo, G. Liu, "The dielectric properties and microstructure of $BaTiO_3$ ceramics with ZnO-Nb_2O_5 composite addition", *J. Alloys Compd*., **646** (2015) 748–752.
28. T. Wang, L. Jin, C. Li, Q. Hu, X. Wei, D. Lupascu, "Relaxor ferroelectric $BaTiO_3$-$Bi(Mg_{2/3}Nb_{1/3})O_3$ ceramics for energy storage application", *J. Am. Ceram. Soc*., **98** (2015) 559–566.
29. Y. Wang, X. Chen, H. Zhou, L. Fang, L. Liu, H. Zhang, "Evolution of phase transformation behavior and dielectric temperature stability of $BaTiO_3$-$Bi(Zn_{0.5}Zr_{0.5})O_3$ ceramics system", *J. Alloys Compd*., **551** (2013) 365–369.
30. X. Wang, R. Huang, Y. Zhao, Y. Zhao, H. Zhou, Z. Jia, "Dielectric and tunable properties of Zr doped BST ceramics prepared by spark plasma sintering", *J. Alloys Compd*., **533** (2012) 25–28.
31. R. Rani, S. Singh, J.K. Juneja, K.K. Raina, C. Prakash, "Dielectric properties of Zr substituted BST ceramics", *Ceram. Int*., **37** (2011) 3755–3758.
32. H. Zhao, X. Duan, T. Yu, D. Xu, W. Zhao, "Enhanced energy storage efficiency of $Ba_{0.8}Sr_{0.2}TiO_3$ ceramics modified by $BiTaO_3$", *Solid State Commun*., **360** (2022) 115050.
33. Z. Liu, Z. Tang, S. Hu, D. Yao, F. Sun, D. Chen, X. Guo, Q. Liu, Y. Jiang, X. Tang, "Excellent energy storage density and efficiency in lead-free Sm-doped $BaTiO_3$-$Bi(Mg_{0.5}Ti_{0.5})O_3$ ceramics", *J. Mater. Chem. C*, **8** [38] (2020) 13405–13414.
34. Y. Chen, Y. Qi, D. Zhao, X. He, Y. Wang, Q. Zheng, D. Lin. "High energy storage density and efficiency in $(Bi_{0.5}Na_{0.5})_{0.94}Ba_{0.06}TiO_3$-based ceramics with broadened and flattened dielectric peaks", *Ceram. Int*., **48** (2022) 30066–30077.
35. J. Li J. Li, S. Qin, X. Su, L. Qiao, Y. Wang, T. Lookman,

Y. Bai. "Effects of long- and short-range ferroelectric order on the electrocaloric effect in relaxor ferroelectric ceramics", *Phys. Rev. Appl.*, **11** (2019) 044032.
36. X. Huang, Y. Yang, R. Wang, F. Tan, W. Cao, X. Wen. C. Wang, "Enhanced energy storage properties of $Bi(Ni_{1/2}Zr_{1/2})O_3$-modified $BaTiO_3$-based ceramics", *J. Mater. Sci. Mater. Electron.*, **34** (2023) 201.
37. W. Qiao, J. Mei, M. Bai, J. Xu, Y. Gao, X. Zhu, Y. Hu, Y. Li, X. Hao, X. Lou, "Enhanced energy storage properties in BNST-based lead-free relaxor ferroelectric ceramics achieved via a high-entropy strategy", *Scr. Mater.*, **243** (2024) 115966.
38. D. Zheng, R. Zuo, "Enhanced energy storage properties in $La(Mg_{1/2}Ti_{1/2})O_3$-modified $BiFeO_3$-$BaTiO_3$ lead-free relaxor ferroelectric ceramics within a wide temperature range", *J. Eur. Ceram. Soc.*, **37** [1] (2017) 413–418.